Theory of interferometric data processing

Christian A. Hummel

European Southern Observatory, Karl-Schwarzschild-Str. 2, 85748 Garching, Germany

Abstract

In this article I discuss methods and issues of interferometric data processing, i.e. how to compute visibilities from interferograms, correct for systematic errors, and calibrate the data. I conclude with some remarks on interferometric imaging, as it can be considered part of data processing, one step before the analysis using physical models of the target observed.

1 Introduction

The interferometer is a complex apparatus producing interferograms which are sensitive to the degree of mutual coherence, γ, between the two beams it combines. The major contributor to γ is the Fourier transform of the brightness distribution of the astronomical object itself (van Cittert-Zernike Theorem), and it is our goal to extract this quantity, V, which is the complex visibility of the object we want to study, from the interferograms.

However, there are numerous effects which degrade γ, all related to what happens to the light during its passage to the detector through the atmosphere and the telescope optics. In general, degradation related to propagation is calibrated by observing a suitable calibrator star (i.e. an unresolved target nearby and of similar magnitude), and degradation related to the detector is characterized using an incoherent mode of the interferometer.

The exact method used for visibility estimation, and knowledge of the spectral bandpass over which the interferograms are averaged, is important for the comparison of the measurements with visibilities from a model during the astrophysical analysis.

Email address: chummel@eso.org (Christian A. Hummel).
URL: http://www.eso.org/~chummel (Christian A. Hummel).

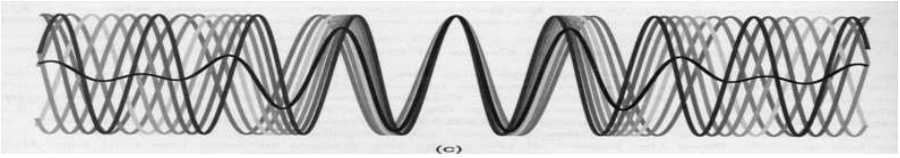

Fig. 1. Idealized white light interferogram (thin line), combining light from seven individual channels. The fringe amplitude drops rapidly with distance from the central white light fringe. Note the phase shift across the bandpass away from the white light fringe.

2 Fringe detection and estimators

In order to measure the mututal coherence between the two beams, after compensation of their optical path difference (OPD), relative phase offsets are introduced which produce a pattern of light and dark bands, the so-called fringes. An interferogram records the maximum and minimum levels of intensity, and the visibility amplitude is defined as follows.

$$V = \frac{I_{\max} - I_{\min}}{I_{\max} + I_{\min}}$$

If the two beams are incoherent, i.e. the coherence time over which there exists a stable phase relationship between them is much smaller than the detector integration time, the fringe contrast approaches zero. On the other hand, the visibility amplitude can never be larger than unity, but should approach it for unresolved targets in the absence of any degrading effects such as poor seeing, poor optics, and wide bandwidth. An idealized interferogram is shown in Fig. 1.

Relative phase offsets are introduced by either modulating the delay lines if the beams are combined in the pupil plane, or by utilizing the geometric optical path differences if the beams are combined in the image plane. There are many interferometers using the former method, AMBER on the VLTI uses the latter.

The visibility function is a complex one, and the phase of the visibility can be extracted by defining a fiducial point of the modulation, and measuring the distance of the nearest fringe peak from it in units of the wavelength, multiplying by 2π. The fringe phase is usually corrupted by the atmospheric fringe motion, unless closure phases are computed.

In the following, I will discuss the three cases of fringes being tracked, usually by detecting a single fringe, of fringe packets being scanned, in which case they are centered, and finally, of interferograms which are imaged onto a two-dimensional detector.

Let us proceed from the simple to the more complicated. In a Michelson interferometer which modulates the delay in a sawtooth pattern, the photon count rate can be measured in four equal sized phase bins (A, B, C, and D) covering exactly one fringe at the wavelength of observation. Then it can be shown that an unbiased estimator exists for the square visibility amplitude as follows (Shao et al. , 1988).

$$V^2 = \frac{\pi^2}{2} \frac{< X^2 + Y^2 - N >}{< N - D >^2}, \tag{1}$$

where $X = A - C$ and $Y = B - D$ are the real and imaginary parts of the Fourier transform of the bin counts, $N = A + B + C + D$ is the total number of counts, and D is the back ground count rate (see Sec. 3). The brackets denote an average, which is done for nominator and denominator separately. This estimator is unbiased only if the detected photon events follow a Poisson distribution, in which case the variance of the signal x, $var(x) \equiv E(x^2) - E(x)^2 = \overline{x}$. Therefore, we show that the bias is exactly N as follows.

$$\begin{aligned}
E(X^2 + Y^2) &= E(X^2) + E(Y^2) \\
&= E((C - A)^2) + E(Y^2) \\
&= E(C^2 - 2CA + A^2) + E(Y^2) \\
&= E(C^2) - 2E(CA) + E(A^2) + E(Y^2) \\
&= \overline{C}^2 + \overline{C} - 2\overline{CA} + \overline{A}^2 + \overline{A} + E(Y^2) \\
&= (\overline{C} - \overline{A})^2 + (\overline{D} - \overline{B})^2 + \overline{A} + \overline{B} + \overline{C} + \overline{D} \\
&= \overline{X}^2 + \overline{Y}^2 + \overline{N}.
\end{aligned}$$

As an example of squared visibilities computed this way for the Navy Prototype Optical Interferometer (NPOI), we show in Fig. 2 that at low amplitudes, even negative (squared) values can exist. This is because the squared visibilities are not the result of a mathematical operation to square a quantity, but the result of Eq. 1 in which a negative result can be obtained if the bias correction (N) is slightly bigger than the term $X^2 + Y^2$. Therefore, a bias would actually be introduced into the results if positivity of the squared visibilities would be enforced.

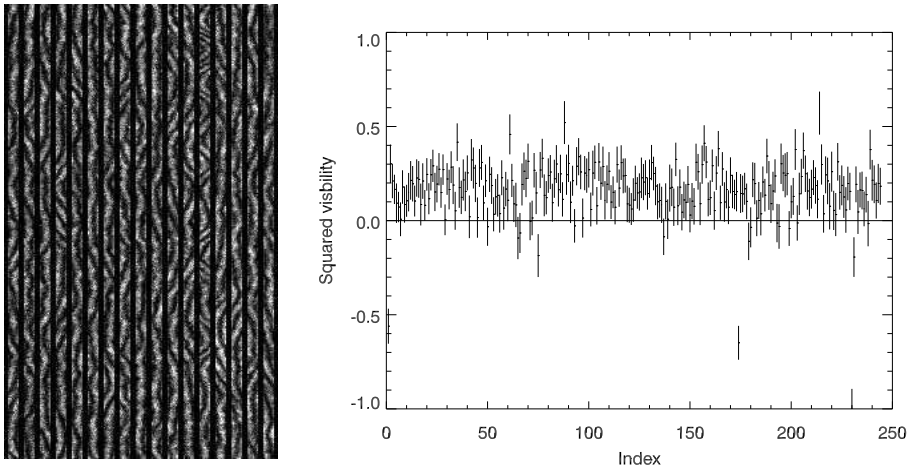

Fig. 2. Fringes and measurements of the squared visibility. On the left, photon count rates as a function of bin phase and time are displayed in grey scale. In each vertical strip, continued by its neighbor to the right, times runs from top to bottom (about 0.8 s), and the width of each strip is one fringe. The fringe tracker employed uses the so-called group delay method, which allows for small systematic residual motion of the fringes as compared to a phase tracking interferometer, where the interferogram is stabilized within the limits of phase noise, albeit at a loss of sensitivity. On the right, showing squared visibility amplitudes, each data point corresponds to an average of 1s. The error bars were computed as errors of the mean based on Gaussian error propagation. Note that there are negative values, of which some are outliers, others are normal statistical fluctuations.

2.2 Fringe scanning

For interferometers without tracking capability, the delay has to be modulated with a larger amplitude to sweep the whole fringe packet across the detector in order to center its peak envelope. Each scan is truncated in post-processing (to exclude the parts not containing fringes) and the power spectral density (PSD) is computed (Fig. 3).

The PSD will peak at the nominal fringe frequency (which is equal to the center wavelength divided by scanning speed) with some power spread around this peak due to atmospherically induced piston (i.e. residuals of the OPD) variations during the longer sweep time, as compared to the single-fringe sweep. Because of this, the PSD is integrated under the peak, rather than just reading off the peak power value. The (square of the) correlated flux thus measured is normalized by the total uncorrelated flux to produce a visibility amplitude, unless the PSD was computed from already normalized interferograms (Kervella et al. , 2004).

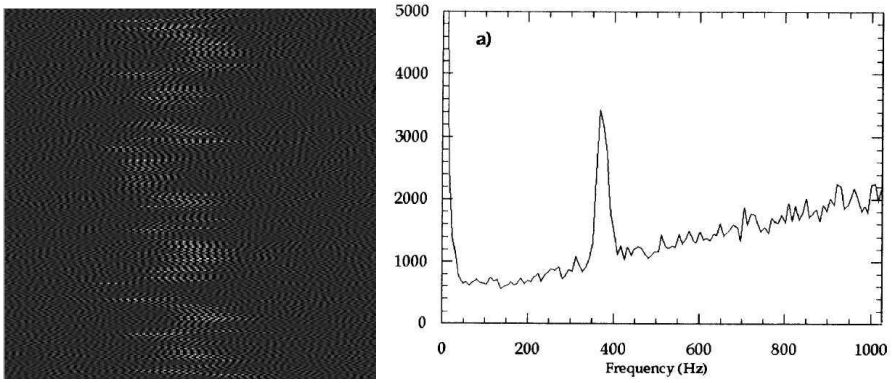

Fig. 3. On the left, a so-called "waterfall" display shows intensity variation as a function of the sweep through the fringe packet (x-axis: OPD), and as a function of time which runs from top to bottom. On the right, the power spectral density of fringes is shown. The fringe signal shows up at the nominal fringe frequency (about 400 Hz), while the tilted baseline is related to the photon noise bias. This bias can be measured by positioning the sweep away from the fringe packet, or just fitting a baseline. The PSD is due to Perrin (2003).

2.3 Fringe modelling

An alternative to the Fourier transform, a model of a fringe can be fit to the actual detector data. This approach is used to extract visibilites from the detector of AMBER, which records 2-dimensional interferograms (spatial versus wavelength space), as shown in Fig 4.

3 Noise sources and visibility bias

Astronomical observations are often carried out at the limit of the equipment sensitivity, and, in the case of interferometers, fringe contrast. The signal to noise ratio of the measurements is a function of both the number of detected photons and the visibility amplitude, therefore one can end up in a regime called "photon starved interferometry" even if the flux is high, but because the visibility is very low. In this regime, photon and detector noise statistics play a very important role.

The detector noise includes read noise (as well as a bias offset in the optical) and dark current. Shot noise, which is produced by the incident photons and which usually follows Poisson statistics, will be discussed here by its effect of causing a variable bias in the measured visibilities. Finally, background photons are an important noise source in the mid-infrared.

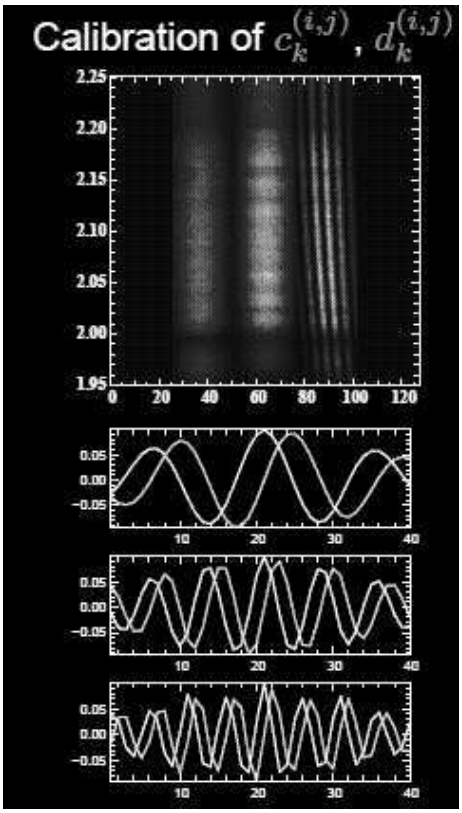

Fig. 4. The figure shows at the top the AMBER detector areas illuminated by two photometric channels, and the interferometric channel (artificial light source, with one of the three beam shutters closed; the third photometric channel would be to the right of the interferometric channel). The dispersion direction is vertical. Fringes are clearly visible and slightly tilted due to an internal OPD offset. Below the image, three panels show the so-called "carrier waves" (i.e. basis functions) corresponding to the three possible spatially encoded fringe patterns (hence their different spatial frequency). Each panel shows a pair of carrier waves 90° apart, corresponding to the sin and cos components of the complex visibility (one wavelength shown only). The fringe model consists of the coefficients of a fit of the carrier waves to the fringe patterns produced by different beam shutter settings. Visibilities of real fringes can then be extracted by multiplying the so-called P2VM coefficient matrix with the pixel intensities of the (cosmetically and DC offset corrected) interferograms.

Even though the noise sources we consider are zero-mean random variables, the visibility is computed as the square modulus so that we may average it in the presence of phase fluctuations caused by the atmosphere. That process converts every noise source into a visibility bias.

3.1 Detector noise

Interferometers typically employ very short integration times (on the order of milliseconds) due to the rapid fringe motion. Read noise, which is a signal-independent noise source added to each read of the detector, is therefore important if CCDs or infrared array detectors are used, while avalanche photo diodes for example do not add read noise. It is typically on the order of a few to ten electrons per pixel read.

If an external fringe tracker allows longer integration times (on the order of seconds), the dark current of IR array detectors has to be measured as well and subtracted from each frame.

3.2 Background

In the mid-infrared, due to the fact that the temperature of a black body radiating predominantly in that wavelength band is comparable to the temperature of the telescope and beam train structure as well as the atmosphere (the detector being cooled), most (on the order of 98%) of the photons received are actually due to background.

3.3 Shot noise

We have already discussed the most simple case of measuring the fringe by counting photons in four equal sized phase bins, assuming Poisson shot noise statistics. Such a case was realized by the Mark III stellar interferometer using photo multiplier tubes, and for the SNR of the squared visibility we have SNR $\approx NV^2$ if $NV^2 > 1$, and SNR $\approx \sqrt{N}V$ if $NV^2 < 1$ (e.g. Shao et al. (1988)). The unbiased measurement of visibilities even very close to the null of a resolved stellar disk is shown in Fig.5 (Quirrenbach et al. , 1996).

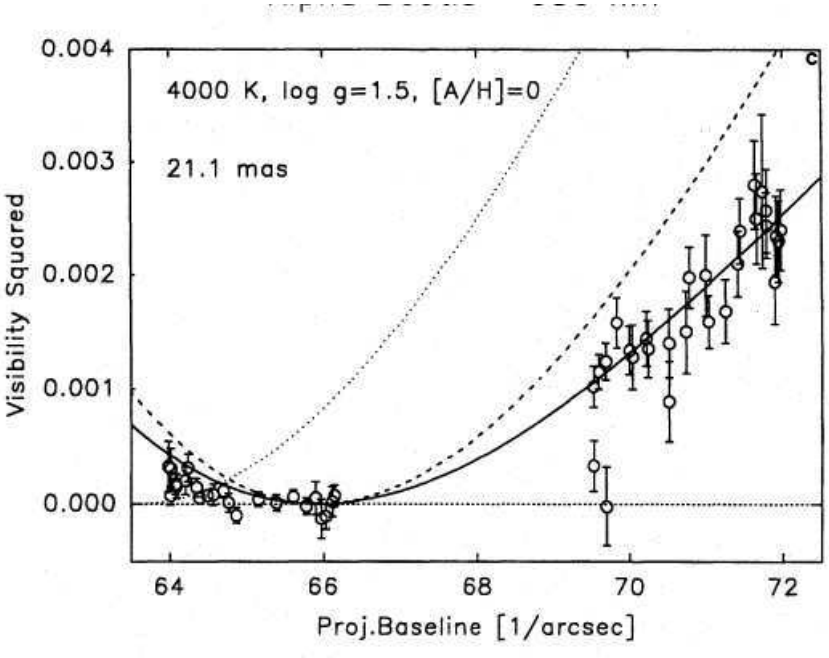

Fig. 5. Measurements of the visibility of a resolved star near the null. Very good bias correction is essential in this measurement.

3.4 Measuring the bias

The total bias is equal to the sum of the variances of each noise source. The latter could be estimated (e.g. in the case of Poisson shot noise), or simply measured as the squared visibility amplitude when the correlated signal is zero (e.g. when offsetting the delay lines from the zero OPD position). Measuring the bias is usually needed because the variances of the noise sources are not easily estimated, and they depend on the target flux. As an example, Fig 6 shows the (squared) visibility amplitudes measured on an incoherent signal.

3.5 Scintillation

If the height of the dominant turbulence layer of the atmosphere is larger than the *Fresnel propagation length* $d_F = r_0^2/\lambda$, the geometric approximation of light propagation is no longer valid and intensity fluctuations will be caused at each telescope in addition to the phase fluctuations. Here r_0 is the Fried parameter (i.e. the seeing), and λ the observing wavelength (see, e.g., Quirrenbach (2000)). Unequal intensities of the interfering beams, I_1 and I_2, would decrease the measured visibility by a factor $\sqrt{I_1 I_2}/(I_1 + I_2)$. This is shown in the following.

Assume two fully coherent ($\gamma = 1$) monochromatic (wavelength λ) beams A

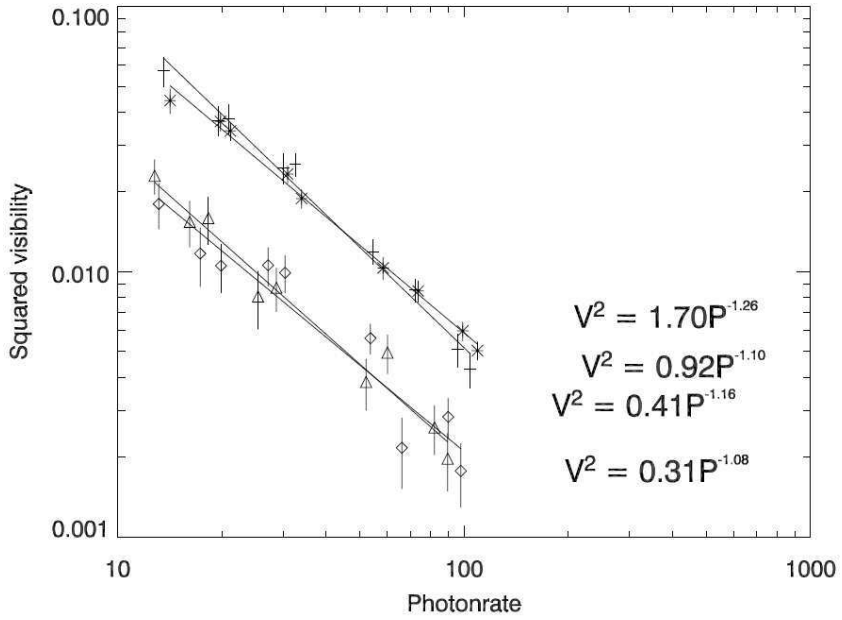

Fig. 6. Measurement of the NPOI visibility bias (in four spectral channels) as function of the photon count rate. Stars of different magnitude have been observed by offsetting the delay lines in order to de-correlate the beams (expected visibility amplitude zero). The bias in each channel (i.e. the measured non-zero visibility amplitude) follows a linear relationship in a log-log plot. Compare the bias levels to the scale in Fig. 5

and B of light with electrical field amplitudes of $A_{\rm A}$ and $A_{\rm B}$. If interferred, their electric field vectors will add, and the total amplitude will vary, as a function of OPD, between $A_{\rm A}+A_{\rm B}$ and $A_{\rm A}-A_{\rm B}$. Since intensity of light is the square of the electric field vectors integrated over a time interval, it will vary between $I^{\rm max}=A_{\rm A}^2+2A_{\rm A}A_{\rm B}+A_{\rm B}^2$ and $I^{\rm min}=A_{\rm A}^2-2A_{\rm A}A_{\rm B}+A_{\rm B}^2$. Therefore, using the definition of the visibility amplitude as $V=(I^{\rm max}-I^{\rm min})/(I^{\rm max}+I^{\rm min})$, the maximum visibility of two interfering beams of intensities $I_{\rm A}$ and $I_{\rm B}$ will be

$$V^{\rm max}=2\frac{\sqrt{I_{\rm A}I_{\rm B}}}{I_{\rm A}+I_{\rm B}}.$$

This visibility will of course be less if the beams are only partially coherent ($\gamma<1$), and the bandwidth of the light is wide.

Scintillation can also be induced by the fluctuating injection of light into a single mode fiber (FLUOR, VINCI, AMBER). Interferometers which do not employ photometric channels in order to calibrate the beam intensity imbalance, can still mostly cancel the effect of scintillation by integrating longer than its typical time scale. It can be shown as follows (D. Mozurkewich, priv. comm.) that because the nominator and denominator of Eq.1 are averaged separately, the intensity ratio fluctuations will not affect the average visibility.

The numerator of Eq. 1 averages to $< N^2V^2 >$ where $N=I_1+I_2$ and

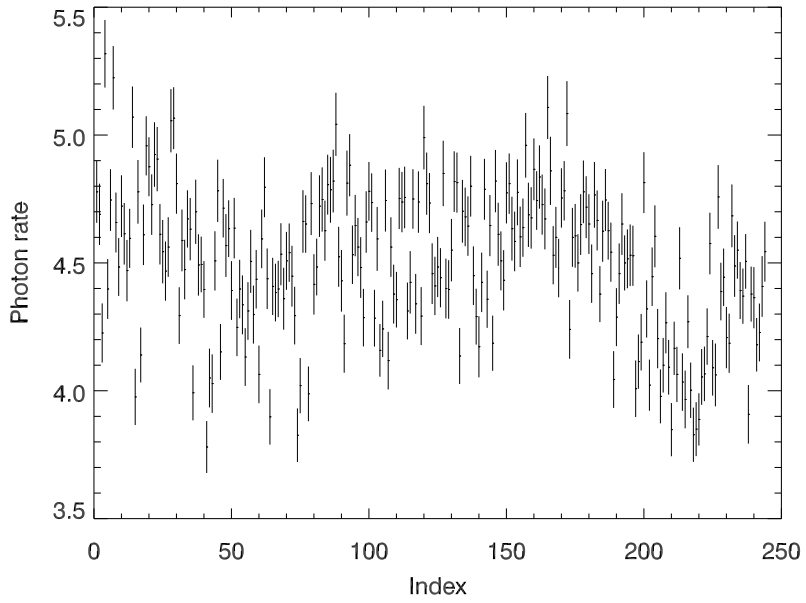

Fig. 7. Scintillation manifesting itself as scatter of the photon count rate larger than the theoretical error bars. The data shown are the number of photons counted by NPOI in a specific spectral channel during a 2 ms interval, averaged over a 1 s interval. The visibility amplitude computed from these data is shown in Fig. 2, and is unaffected by the scintillation.

$V = 2V_0\sqrt{I_1 I_2}/(I_1 + I_2)$ with V_0 the true visibility. Therefore, the mean value of the numerator becomes $4 < I_1 >< I_2 >< V_0 >^2$ if I_1 and I_2 are independent. Thus, only the mean beam intensity ratio causes a reduction in V, but not fluctuations of the mean ratio.

3.6 Observational limits

The limits of observability of targets are of course established by estimating the SNR of the visibility given an integration time. In general, this relationship has not been established yet for the VLTI instruments, but as a proxy the correlated flux can be used to set the limit. In the case that the noise is dominated by a source independent of the signal, e.g. by background in the mid-infrared or by read noise in the NIR, the SNR is proprtional to the correlated flux, NV. Only in the optical, using detectors without read-out noise (e.g. APDs), the SNR of the squared visibility is proportional to NV^2.

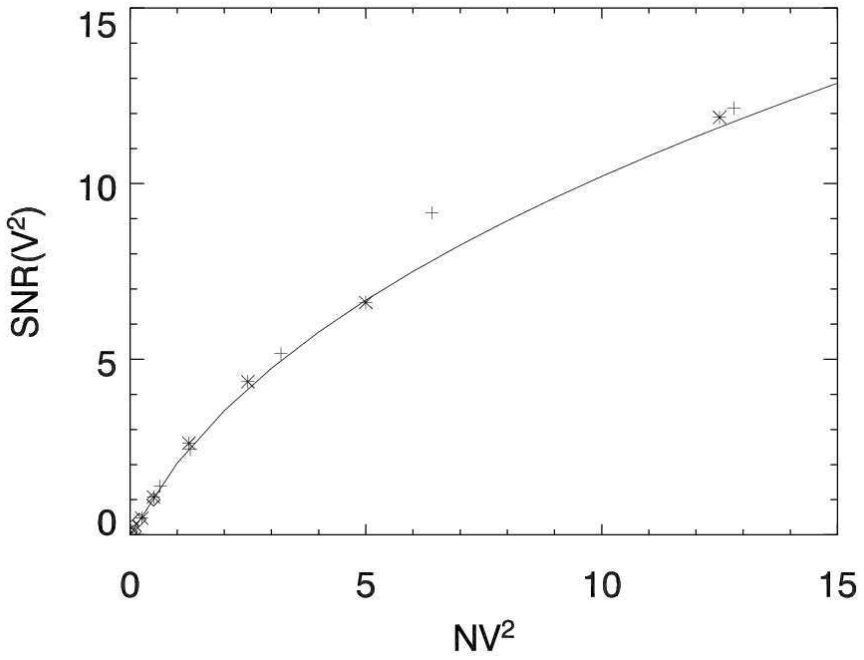

Fig. 8. Squared visibility SNR versus NV^2. The curve corresponds to the theoretical expectation, while the symbols denote the results of a numerical simulation.

4 Advanced techniques

In this section we discuss ways of dealing with some of the limitations set by the atmosphere, be it the short coherence time, the small Fried parameter, or the mid-infrared background.

4.1 Coherent integration and bootstrapping

If the SNR of a single measurement of the squared visibility is less than unity, averaging M samples only increases the SNR by $\sqrt{M}$. However, if one is able to coadd several frames to increase the number of photons N detected in a single coherent average, the SNR increases proportional to N. This is shown in the following equation (Shao et al. , 1988), see Fig. 8.

$$\mathrm{SNR}(V^2) = \frac{1}{4} M^{1/2} N V^2 \left[1 + \frac{1}{2} N V^2\right]^{-1/2}$$

The process of coadding frames is called coherent integration, but requires of course (if done offline) the removal of the atmospheric phase disturbances. A method applied to data of the NPOI has been described in detail by Hummel (2002); another one has been implemented in the EWS data reduction software

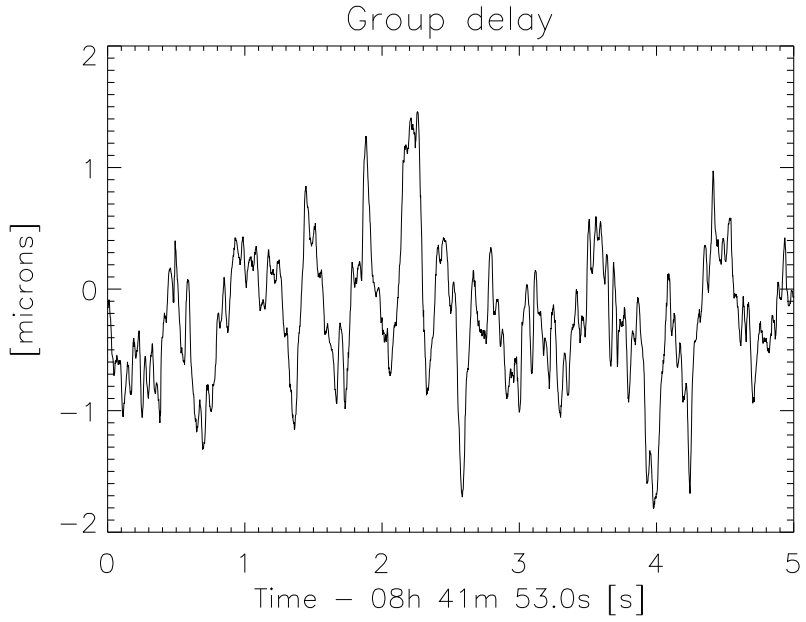

Fig. 9. The residual group delay, after fringe tracking with NPOI (at an effective wavelength of 700 nm).

for MIDI. The general principle is to implement offline fringe phase tracking by which the visibility phasors can be aligned before coadding them (typically a few hundred ms at a time), resulting in an averaged complex visibility. If their SNR is larger than unity, an incoherent average using Eq. 1 is adequate to compute the final squared visibilities. The closure phase would be computed from the vector averaged triple product of the coherent complex visibilities.

Unless the interferometer is equipped with a fringe phase tracker (e.g. FINITO on the VLTI), in which case the coadding can be done in real-time by just increasing the integration time of the interferograms, the deviation of the instantaneous OPD from the OPD of the white light fringe has to be measured for each frame. If the fringes are dispersed, the derivative of the visibility phase with wavenumber determines the offset, and the white light fringe is defined to have a zero derivative. Figure 9 shows an example.

When the complex visibility is multiplied by $e^{2\pi id/\lambda}$, where d is the group delay and λ the wavelength of the channel, the resulting visibility phases are not random anymore, as shown in Fig. 10. However, there is still a systematic variation, and it is shown in the same figure that the phases correlate with the delay residual from the geometrical prediction (piston). The reason for this is that the group delay is more a measure of the position of the peak of the fringe packet envelope, while the different amount of air in the path above each telescope has not only caused a delay difference, but also, due to air dispersion, different phase curvature over the bandpass and therefore slightly different fringe phases with respect to the envelope peak. This is demonstrated

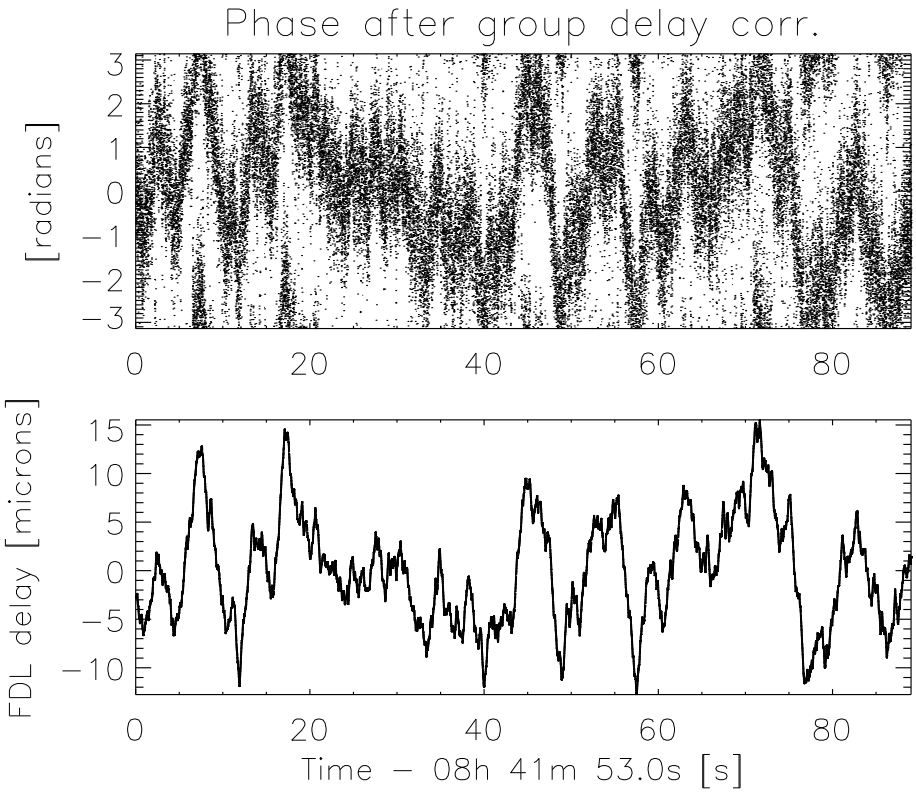

Fig. 10. Top: The visibility phase of the white light fringe (700 nm) after group delay tracking, as a function of time in seconds. Bottom: the residual delay on the same time scale, showing a very good correlation with the phase.

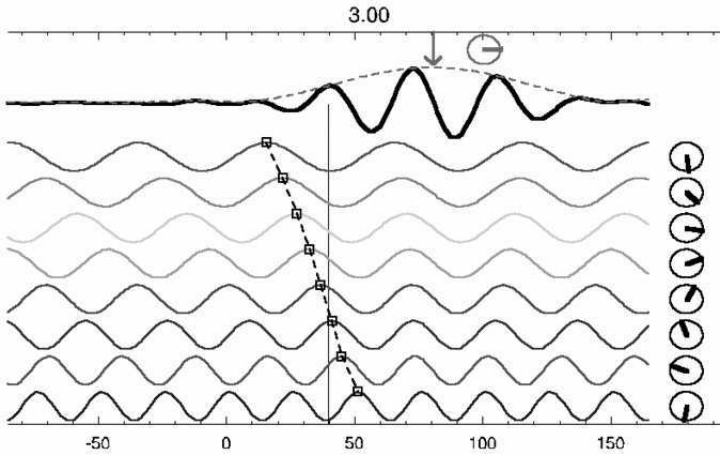

Fig. 11. The effect of air dispersion on the group delay phase(Meisner , 2004). The white light interferogram at the top is the sum of all monochromatic interferograms shown below it. A certain amount of wet air has been introduced and one can see that the peak of the fringe envelope does not coincide with a fringe peak. That difference is called the group delay phase.

in Fig. 11(Meisner , 2004).

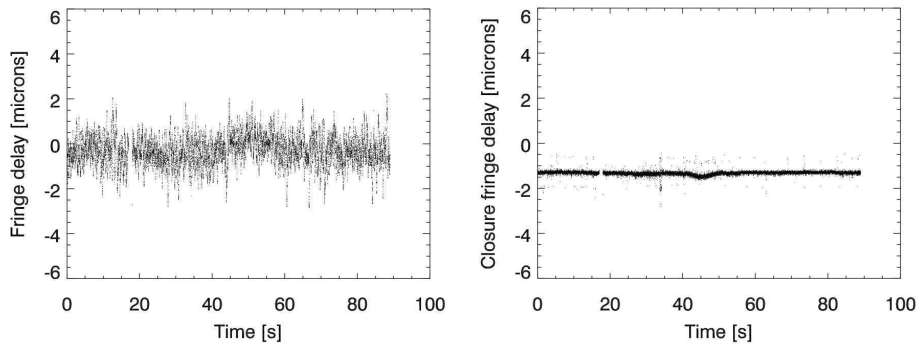

Fig. 12. Left: fringe delay of one of the baselines in a triangle; right: closure fringe delay. Note how all systematic variations have disappeared.

The correction can be derived as follows. The group delay phase is

$$\Phi_d = \frac{2\pi}{\lambda} An - \frac{2\pi}{\lambda} d,$$

where A is the path length difference (between the two beams) through air, n is the refractive index (wavelength dependent), and d is the group delay (including the portion compensated by the delay line). If the refractive index is written as (in good approximation)

$$n = n_0 + \frac{a}{\lambda},$$

with a a constant, then the group delay is equal to An_0. Thus, the group delay phase can be rewritten as

$$\Phi_d = \frac{2\pi}{\lambda^2} \frac{a}{n_0} d.$$

The delay of the white light fringe, the so-called fringe delay, which would have been realized by a real-time phase tracker, can be computed by integrating the group delay phase normalized by the wavelength over the bandpass.

The full power of coherent integration is realized in situations where the fringe delay on a baseline with low SNR can be estimated from the delay on the other two, usually shorter, baselines with which a triangle of baselines is formed. That technique is called baseline bootstrapping and is based on the fact that the sum of the fringe delay on all baselines of a triangle is zero (Fig. 12). As an example, Fig. 13 shows the improvement in the squared visibility on the long bootstrapped E-W baseline of NPOI, in the C-E-W triangle.

Another advantage of coherent integration is that the term $X^2 + Y^2$ in Eq. 1 will dominate N as more photons are detected, decreasing the magnitude of the bias (see this in Fig. 6).

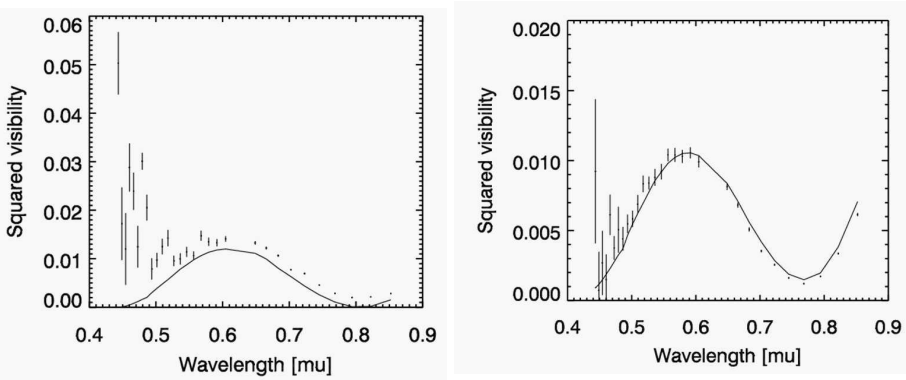

Fig. 13. Squared visibility amplitudes, without (left) and with (right) coherent integration. The coherent integration time was 200 ms, and the incoherent integration was done over a 1 second interval.

4.2 Wavefront filtering

The dependence of the quality of the fringe measurements goes beyond just the atmospheric coherence time, but also includes the Fried parameter r_0, i.e. the typical size of a seeing cell over which the phase of the wavefront does not vary by more than one radian. As is well known, telescopes with an aperture larger than r_0 do not produce an Airy pattern in their focus but rather a speckle pattern, and if used in an interferometer, the visibility will be badly affected by changes in r_0. That is because the individual speckles are mutually incoherent. The number of speckles can be reduced by using adaptive optics. Even then, an elegant method to select just the light which contributes to the coherent flux was invented by Coude du Foresto et al. (1997), and makes use of fibers which transmit only a single mode of light. In other words, at the output of such a fiber, a near perfect Gaussian profile wavefront is made available for beam combination. The seeing fluctuations are instead transformed into flux variations (induced scintillation), which, if some light is picked off from the single mode fiber via a coupler, can be used to accurately normalize the interferograms.

Even if just used after the beam combiner (without the possibility to measure the photometric variations) as in the Palomar Testbed Interferometer (PTI, Colavita (1999)), a significant improvement of the visibilities can be produced, and for the reasons discussed above, only the average intensity ratio between the two arms needs to be corrected for (Shaklan et al. , 1992).

The principle of the normalization of the interferograms can be outlined as follows (see Kervella et al. (2004)). First, the coefficients of the so-called κ matrix relating intensities on the output side of the beam combiner ($I_{1,2}$) with

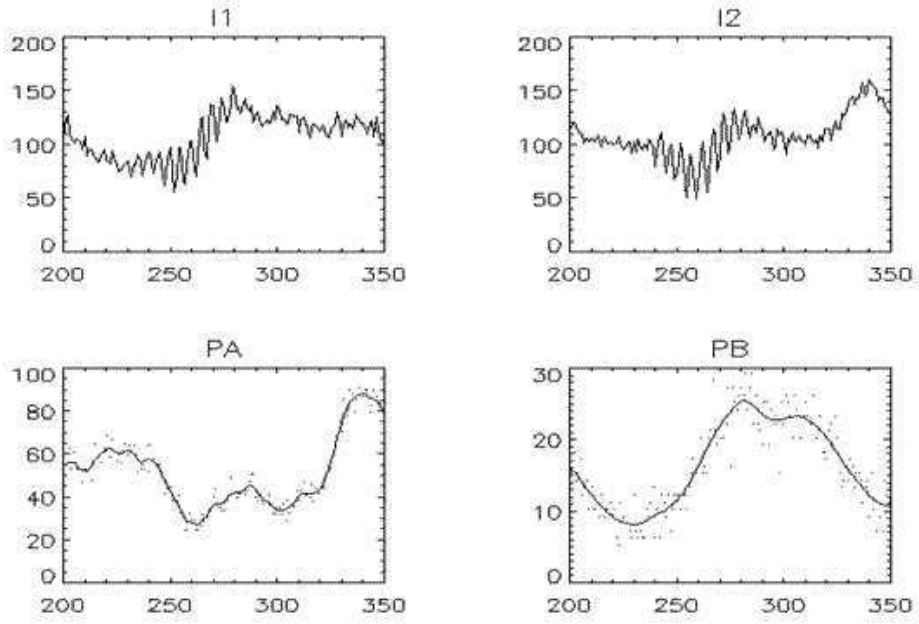

Fig. 14. Raw interferometric signals I_1 and I_2, as well as simultaneous photometric signals P_A and P_B The curves fitted to the photometry are the result of the application of a Wiener filter.

the input intensities ($P_{\mathrm{A,B}}$) need to be determined. Then we have

$$I_1 = \kappa_{1,\mathrm{A}} P_\mathrm{A} + \kappa_{1,\mathrm{B}} P_\mathrm{B}$$

and

$$I_2 = \kappa_{2,\mathrm{A}} P_\mathrm{A} + \kappa_{2,\mathrm{B}} P_\mathrm{B}.$$

As one can see in Fig 14, a good fraction of the fluctuating interferometric signal is due to the fluctuations in the coupling efficiency into the fiber, expressed in the intensities in the photometric channels P_A and P_B. They can optionally be smoothed using a Wiener filter. Then the normalization of the interferometric signals I_1 and I_2 is performed as follows.

$$I_{1,\mathrm{cal}} = \frac{1}{2\sqrt{\kappa_{1,\mathrm{A}}\kappa_{1,\mathrm{B}}}} \frac{I_1 - \kappa_{1,\mathrm{A}} P_\mathrm{A} - \kappa_{1,\mathrm{B}} P_\mathrm{B}}{< \sqrt{P_\mathrm{A} P_\mathrm{B}}]_{\mathrm{Wiener}}}$$

$$I_{2,\mathrm{cal}} = \frac{1}{2\sqrt{\kappa_{2,\mathrm{A}}\kappa_{2,\mathrm{B}}}} \frac{I_2 - \kappa_{2,\mathrm{A}} P_\mathrm{A} - \kappa_{2,\mathrm{B}} P_\mathrm{B}}{< \sqrt{P_\mathrm{A} P_\mathrm{B}}]_{\mathrm{Wiener}}}$$

The resulting signals are shown in Fig 15; they still show some residual background fluctuation, which, however, correlates quite well between the two interferometric outputs and thus can be eliminated by subtracting one from the other.

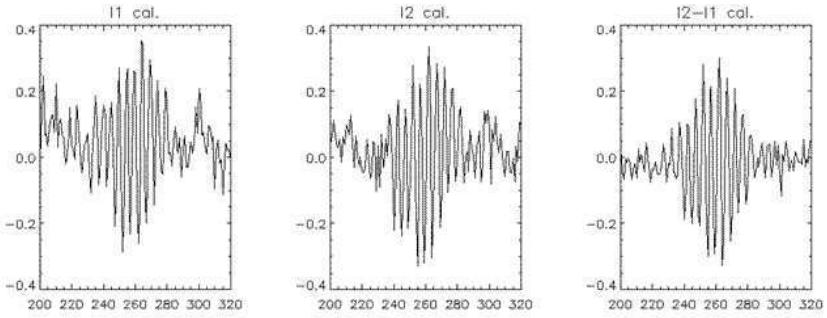

Fig. 15. Normalized interferometric signals $I_{1,\mathrm{cal}}$ and $I_{2,\mathrm{cal}}$, and their difference showing no residual background and fiber injection fluctuations.

4.3 Mid-infrared background elimination

Interferometry in the mid-infared with VLTI/MIDI is at the forefront of technology due to the difficulties of dealing with the background emission. For a long time, only one other interferometer, ISI, has been able to produce science-grade visibilities in this regime, but due to the detection method, using heterodyne radio techniques, the sensitivity is very limited. Now, also the Keck Interferometer has obtained scientific results in the mid-infrared.

Aside from the obvious cooling of detector and beam combination optics, the proper transfer of the telescope pupil onto the entrance window of MIDI and the subtraction of the two beam combiner outputs help to eliminate most of the background fluctuations. This is because the background fluctuations are highly correlated between the beam combiner outputs, while the relative fringe phase is 180 degrees. In order to acquire the targets, standard on-source/off-source chopping techniques are used to remove the background.

The intensity of light in the two interferometric channels of MIDI can be written as (here for I_1 only)

$$I_1 = I_{\mathrm{A},1} + I_{\mathrm{B},1} + (1/2)(I_1^{\max} - I_1^{\min}) \sin(2\pi OPD/\lambda)$$

where $(1/2)(I_1^{\max} - I_1^{\min})$, the intensity variation due to interference, is equal to $2\sqrt{I_{\mathrm{A},1} I_{\mathrm{B},1}} V$. Due to the beam splitter, $I_{\mathrm{A},1} = \kappa_{1,\mathrm{A}} I_A$, where I_A is the intensity in the photometric channel A, and so forth, defining the coefficients of the so-called κ-matrix.

An interferogram, i.e. the intensity as a function of OPD of a single scan across the fringe packet free from background variations, is derived as mentioned above by computing $I_1 - I_2$. The background will be greatly reduced to $I_{\mathrm{A}}(\kappa_{1,\mathrm{A}} - \kappa_{2,\mathrm{A}} + \alpha(\kappa_{1,\mathrm{B}} - \kappa_{2,\mathrm{B}}))$ where α is the ratio of the beam intensities from the two telescopes. The fringe signals, however, will add, to become $2V\sqrt{I_{\mathrm{A},1} I_{\mathrm{B},1}} + 2V\sqrt{I_{\mathrm{A},1} I_{\mathrm{B},1}}$.

The correlated flux derived from the interferogram $I_1 - I_2$ has to be normalized by the total flux, and for that purpose, MIDI takes two photometric exposures (HIGH_SENS mode), one with shutter A open, the other with shutter B. The resulting spectra $I_{\mathrm{AB},12}$ can be used directly to compute the normalization factor $\sqrt{I_{\mathrm{A},1} I_{\mathrm{B},1}} + \sqrt{I_{\mathrm{A},2} I_{\mathrm{B},2}}$, by which the correlated flux, computed from the interferogram $I_1 - I_2$ has to be divided.

With MIDI, the beam combiner can be changed to one where simultaneous photometric channels are recorded (SCI_PHOT mode), and it is only necessary to determine the coefficients of the κ-matrix on any bright target to compute the coefficients of the κ-matrix, as follows: $\kappa_{1,\mathrm{A}} = I_1/(I_1 + I_2)$, $\kappa_{2,\mathrm{A}} = I_2/(I_1 + I_2)$, and so forth. (Therefore, it does not matter whether the photometry exposures are done using the HIGH_SENS or SCI_PHOT beam combiners.) The κ-matrix coefficients can then be used to compute the $I_{\mathrm{AB},12}$ from the spectra $P_{\mathrm{A,B}}$ determined from the photometric channels. The advantages of this mode include the simultaneity of fringe and photometric exposures (while chopping), and elimination of any beam overlap changes between fringe and photometric exposures taken at different times.

5 Calibration and error estimates

Due to the dependency of the performance of an interferometer on the ambient and atmospheric conditions, the observations for the calibration of the scientific data have to be performed near simultaneously with the latter. Stars with a known diameter or a diameter small enough to be irrelevant are observed, and the resulting visibility amplitude is known as the transfer function, system visibility, or interferometric efficiency of the interferometer. Normally, the visibility amplitude measured on a science target would be divided by the amplitude measured for the calibrator in order to derive a calibrated visibility.

However, it is educational to keep in mind that an approach far better would be to characterize the dependency of the transfer function on the seeing (or other atmospheric and instrumental properties), and then to transfer that parametrization to the science target. This has only worked routinely with one interferometer, namely the Mark III Stellar Interferometer, which used 5 cm apertures and therefore was never used in the multi-speckle mode (Fig. 17). That interferometer apparently also had the least instrumental effects on the visibility, since the seeing calibration was often the only one needed.

If, during a night, several calibrators have been observed with the same instrumental setup, comparison between them will indicate the quality of the night, and will also give a conservative estimate of the calibration error. However, it is still advisable to not use an average transfer function for calibration but

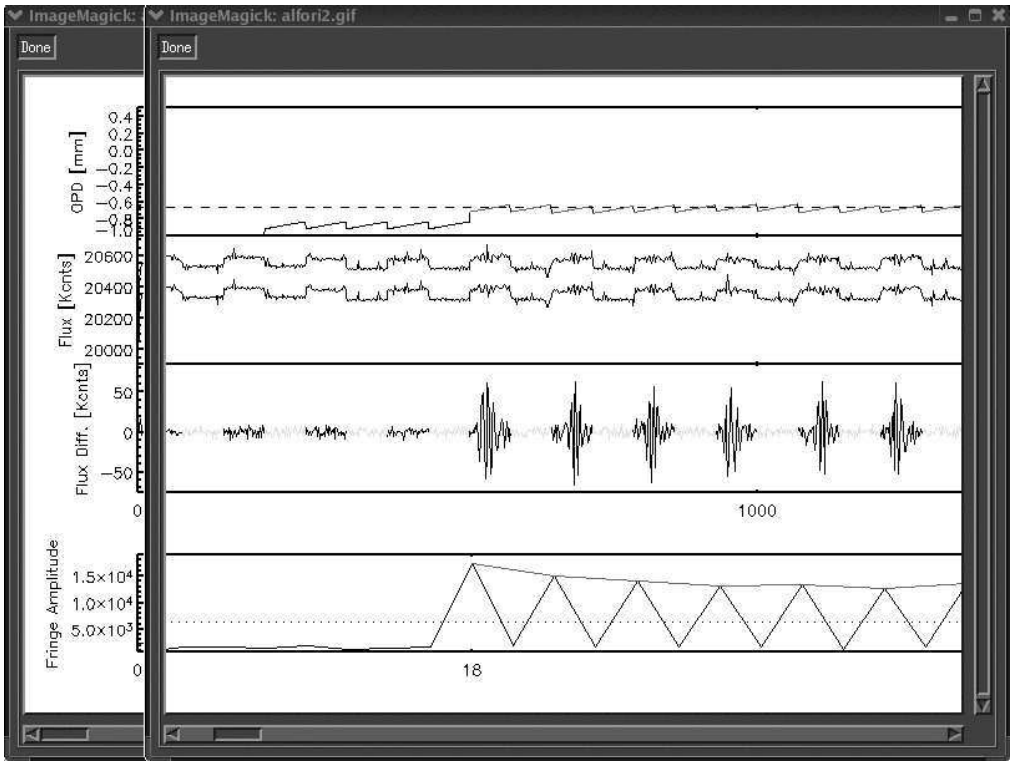

Fig. 16. Reduction of MIDI data taken with the SCI_PHOT beam combiner and simultaneous fringe centering and chopping. Display of the XMDV GUI of the MIA software (*http://www.strw.leidenuniv.nl/~nevec/MIDI/index.html*) showing in the top panel the OPD modulation, then the signals of the two interferometric channels, then the difference between the two revealing the interferograms, and finally, the visibility amplitudes derived from each interferogram. Note that this target, α Orionis, is bright enough to produce a noticable step in the total background dominated signal while chopping.

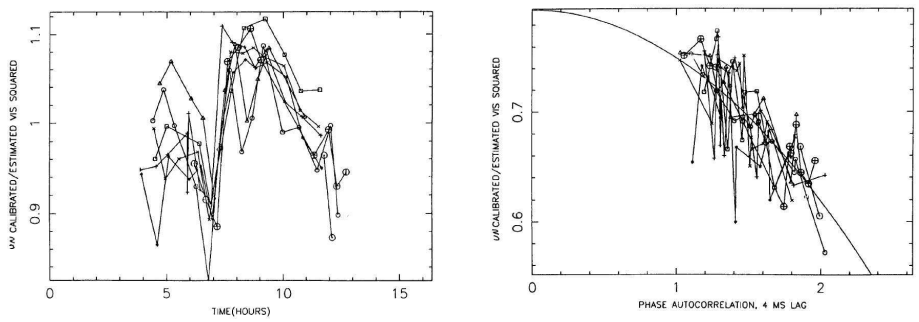

Fig. 17. Left: calibrator visibilities measured in a particular night with the Mark III interferometer. Right: the correlation of the visibility with a seeing index. All calibrators are consistent with the same parameterization, indicated by the fit.

rather the calibrator foreseen for the particular science target, due to changing conditions and the better match in brightness (we presume).

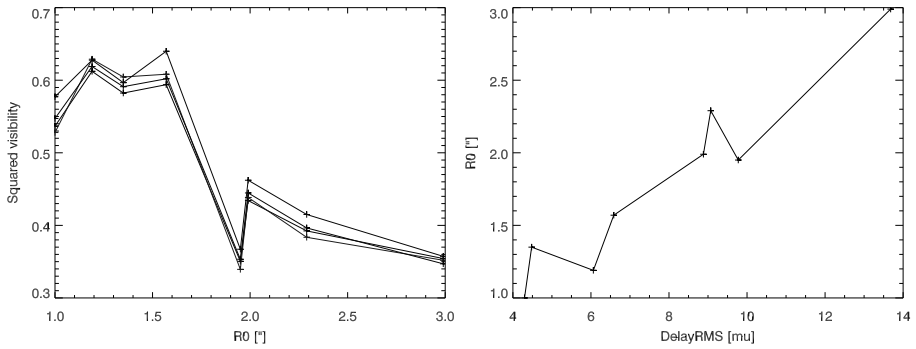

Fig. 18. Dependence of MIDI visibility on seeing, and the correlation between r_0 and the RMS of the delay.

6 Interferometric imaging

From a model fitting point of view, interferometric imaging amounts to no more than fitting a number of pixel intensities to the visibility data, whereby the only constraint on the model is the positivity of the pixels. This process is based on the fact that the complex visibility function is the Fourier transform of the object brightness distribution (van Cittert-Zernike theorem). It is immediately obvious that due to the typically much larger number of pixels compared to a few model parameters, the amount of data needed to make this process converge to a reasonably well constrained solution is rather large. However, since it is the stated ultimate purpose of interferometers to synthesize a larger aperture, imaging has become the standard product of radio interferometers. In the optical, imaging is still the exception, due to the very sparse arrays and limited observing time.

Since the visibility phases in the radio suffer, just as in the optical, from random fluctuation due to the propagation through the ionosphere and atmosphere, methods to self-calibrate the phase data had been developed already quite some time ago. Because the closure phase is not corrupted by the atmosphere, one can simply go through all independent triangles, assign the closure phase to one of its baselines not set before (if any, and subtracting the sum of the phases already assigned to the other two baselines) and thus store all known phase information in the $n(n-1)/2$ baselines, preserving the closure relations.

Then, in an iterative manner, the missing phase information is replaced by phases predicted by the model, and since the model is improved in each iteration, so is the model prediction, eventually the predicted phase are no different than what would have been measured. The model is improved in each iteration by using an algorithm deconvolving the Fourier transform of the hybrid data set from the "dirty" PSF synthesized by the *uv*-coverage, ideally placing flux only into those pixels of the deconvolved image where real flux is indicated.

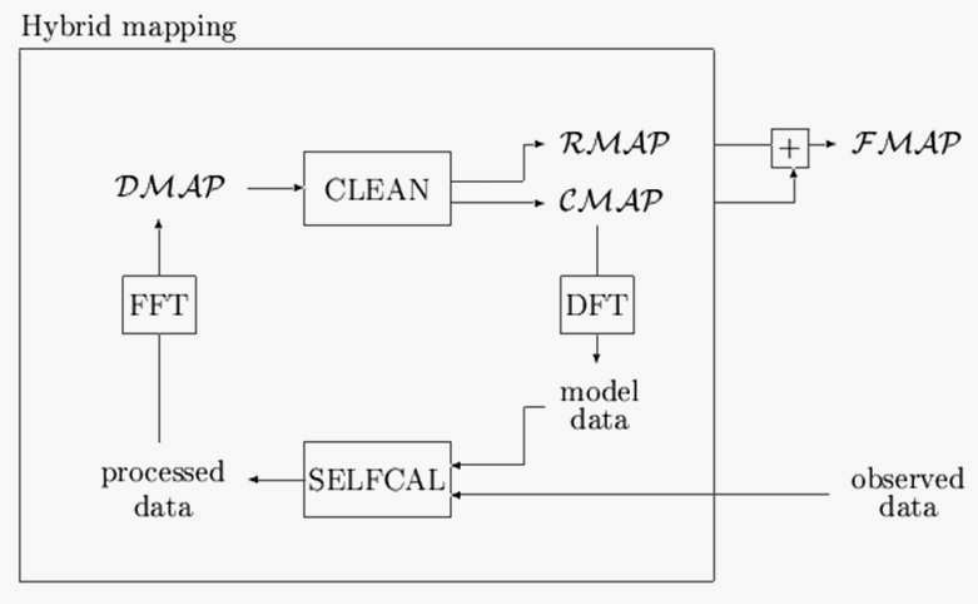

Fig. 19. Hybrid mapping scheme. SELFCAL adjusts station based phase terms to match model and observed data, which is Fourier transformed to yield the "dirty" map (DMAP). CLEAN devonvolves DMAP from the synthesized PSF to yield a "clean" (CMAP) and residual map (RMAP). CMAP delivers the updated model visiblities via a direct Fourier transform. After a few iterations, RMAP and CMAP are combined for the final map (FMAP).

Taking, for example, the CLEAN algorithm, the correlation of the dirty image with the dirty PSF is computed, whose maximum will always coincide with a pixel containing some fraction of real flux.

This process converges if the source structure is sufficiently simple, and since real flux, when removed from the model for purposes of testing the reality of certain features, will return after a few iterations, some confidence can be obtained on the structures mapped. Synthesis imaging in the radio is described in more detail by Perley et al. (1989). The algorithms are partly applicable also to optical interferometry data, however, the use of squared visibility amplitudes and closure phase make dedicated imaging software more desirable, and a first package has been released to the community (BSMEM: *http://www.mrao.cam.ac.uk/research/OAS/bsmem.html*).

An interesting problem arises if one tries to combine the data of all channels in an interferometer dispersing the light in order to improve the usually very sparse *uv* coverage. That is because of the likely dependence of the target structure on wavelength. If that dependence can be parameterized easily, e.g. with the effective temperature in applications involving normal stars, it may be assigned as an additional property of the CLEAN component and then taken into account when computing the model visibilities. For that purpose, a modified version of the mapping process called Difference Mapping can be employed which allows for a more rapid update of the corrected data.

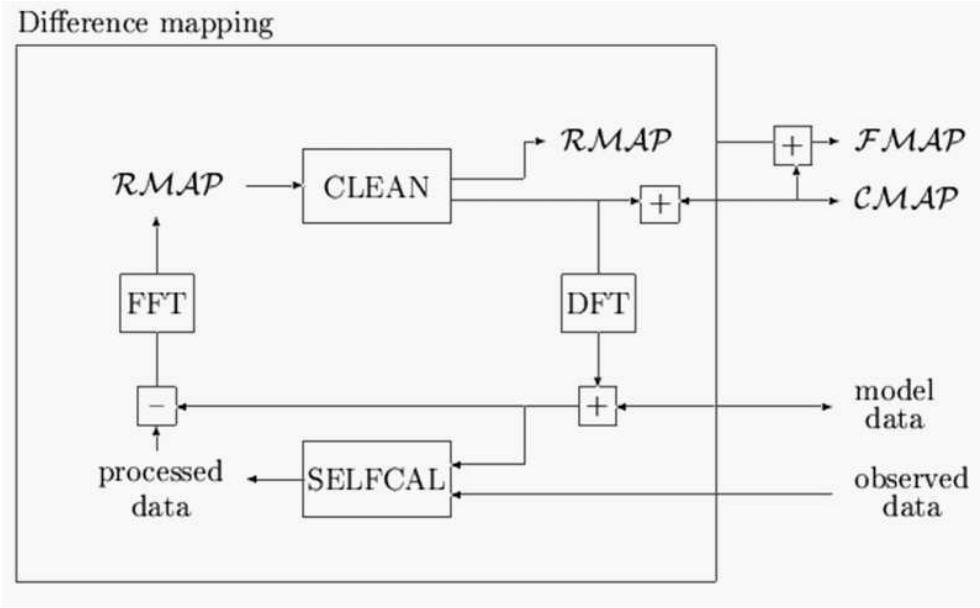

Fig. 20. Difference mapping scheme: the model components are accumulated over several full iterations, each time performing CLEAN on the residual map only, i.e. the difference between the Fourier transform of all data and the transform of the current model.

References

Colavita, M. M., Fringe visibility estimators for the Palomar Testbed Interferometer, 1999, PASP, 111, 111

Coude Du Foresto, V., Ridgway, S., & Mariotti, J.-M., Deriving object visibilities from interferograms obtained with a fiber stellar interferometer, 1997, A&AS, 121, 379

Hummel, C.A., Mozurkewich, D., Benson, J. A., & Wittkowski, M., Coherent integration using phase bootstrapping, 2002, in Interferometry for Optical Astronomy II, ed. W. Traub, Proceeding of SPIE Vol. 4838 (SPIE: Bellingham), p. 1107

Kervella, P., Sègransan, D., & Coudè du Foresto, V., Data reduction methods for single-mode optical interferometry, 2004, A&A 425, 1161

Lawson, P. R., Cotton, W. D., Hummel, C. A., et al., An interferometry imaging beauty contest, 2004, in New Frontiers in Stellar Interferometry, ed. by W. Traub, Proceedings of SPIE Vol. 5491 (SPIE: Bellingham), p. 886

Meisner, J., Conceptual Design Review PRIMA Astrometry Operations and Software, 2004, *http://www.strw.leidenuniv.nl/∼meisner/*, with permission.

Perley, R.A., Schwab, F.R., & Bridle, A.H. 1989, Synthesis imaging in radio astronomy, A collection of lectures of the third NRAO synthesis imaging school (Astronomical Society of the Pacific: San Francisco)

Perrin, G., Subtracting the photon noise bias from single-mode optical interferometer visibilities, 2003, A&A, 398, 385

Quirrenbach, A., Mozurkewich, D., Buscher, D. F., Hummel, C. A., Arm-

strong, J. T., Angular diameter and limb darkening of Arcturus, 1996, A&A, 312, 160

Quirrenbach, A., Observing through the turbulent atmosphere, in Principles of Long Baseline Stellar Interferometry, ed. by P. Lawson, JPL Publication 00-009, 2000, p. 71

Shaklan, S. B., Colavita, M. M., & Shao, M., Visibility calibration using single mode fibers in a long-baseline interferometer, 1992, in High-resolution imaging by interferometry II, eds. J. M. Beckers and F. Merkle (ESO: Garching), p. 1271

Shao, M., Colavita, M. M., Hines, B. E., Staelin, D. H., Hutter, D. J., Johnston, K. J., Mozurkewich, D., Simon, R. S., Hershey, J. L., Hughes, J. A., Kaplan, G. H., The Mark III stellar interferometer, 1988, A&A, 193, 357